

# A Moving Mesh Method for Porous Medium Equation by the Onsager Variational Principle

Si Xiao<sup>a</sup>, Xianmin Xu<sup>b,c,\*</sup>

<sup>a</sup> School of Mathematics and statistics, Fuzhou Univeristy, Fuzhou, 350108, China

<sup>b</sup> State Key Laboratory of Mathematical Sciences, Academy of Mathematics and Systems Science, Chinese Academy of Sciences, Beijing, 100190, China

<sup>c</sup> School of Mathematical Sciences, University of Chinese Academy of Sciences, Beijing, 100049, China

---

## Abstract

In this paper, we present a novel moving mesh finite element method for solving the porous medium equation, using the Onsager variational principle as an approximation framework. We first demonstrate that a mixed formulation of the continuous problem can be derived by applying the Onsager principle. Subsequently, we develop several numerical schemes by approximating the problem within a nonlinear finite element space with free knots (movable nodes), following the same variational approach. We rigorously prove that the energy dissipation structure is preserved in both semi-discrete and fully implicit discrete schemes. Additionally, we propose a fully decoupled explicit scheme, which requires only the sequential solution of a few linear equations per time step. Other variants of the method can also be derived analogously to preserve mass conservation or to enhance stability. The numerical schemes achieve optimal convergence rates when the initial mesh is carefully chosen to ensure good approximation of the initial data. Through extensive numerical experiments, we evaluated and compared the efficiency and stability of the proposed schemes with existing approaches. For cases involving uniform initial meshes, all schemes exhibit good stability, with the fully decoupled scheme demonstrating superior computational efficiency. In contrast, when addressing singular problems on nonuniform meshes, the stabilized explicit scheme strikes a good balance between stability and computational efficiency. In addition, the method inherently captures the waiting time phenomenon without requiring user intervention, further illustrating its robustness.

*Keywords:*

Porous medium equation, Onsager variational principle, moving mesh method

---

## 1. Introduction

The porous medium equation (PME) serves as a prominent mathematical model frequently utilized to comprehensively describe various physical and biological phenomena, including gas flow, nonlinear heat transport, groundwater movement, etc. The PME is a nonlinear partial differential equation taking the form:

$$\partial_t \rho = \Delta \rho^m, \quad m > 1. \quad (1)$$

Extensive research has revealed numerous intriguing properties of this equation. One particularly fascinating characteristic is its association with a finite speed of propagation. This stands in stark contrast to the linear heat equation ( $m = 1$ ), where heat propagation speed is infinite. Notably, if the initial value of  $\rho$  possesses compact support, the boundary of this support moves at a finite velocity even when the equation is defined across the entire space, leading to

---

\*Corresponding author

\*\*Funding: The work was partially supported by the National Natural Science Foundation of China(Grant No. 12371415 and 12461160275), and by Beijing Natural Science Foundation (Grant No. Z240001).

Email addresses: xiaosi@lsec.cc.ac.cn (Si Xiao), xmxu@lsec.cc.ac.cn (Xianmin Xu)

9 a typical free boundary problem. Furthermore, under specific initial conditions, the solution of the PME may demon-  
10 strate a waiting time phenomenon [? ], wherein the free boundary remains stationary until a critical time threshold is  
11 surpassed. These properties have been extensively investigated in mathematics (e.g in [? ? ? ? ? ]).

12 From a numerical perspective, solving the PME presents several challenges. Firstly, the free boundary of the  
13 solution is not easy to captured by standard numerical methods. The moving velocity of the boundary depends on the  
14 derivative of the solution. To ensure precise velocity calculations, it is imperative to compute the gradient velocity with  
15 precision. Secondly, singularities in the solution of the PME arise at the free boundary. For larger  $m$ , the regularity is  
16 worse. Thirdly, it is also a challenge to accurately compute the waiting time.

17 These challenges have sparked significant interest in the PME, leading to the development of numerous numerical  
18 methods in literature. In early investigations, researchers commonly transformed the PME into an alternative equation  
19 based on pressure, which exhibits better regularity. The free boundary was typically addressed using either a front  
20 tracing method or by extending the equation to a larger fixed domain to avoid boundary issues. The pressure equation  
21 was often solved using a finite element method [? ] or a finite difference method [? ? ? ? ], yielding a convergence  
22 rate typically of first order with respect to the mesh size. Later on, the original PME was solved by using a high order  
23 local discontinuous Galerkin method to improve the accuracy. A suitable non-negativity preserving limiter was used  
24 to prevent oscillations near the free interface [? ]. More recently, new numerical schemes have emerged for the PME,  
25 focusing on preserving the positivity of density and the energy dissipation relation [? ? ].

26 Given the singularity and moving boundary present in the solution of the PME, a natural approach is to employ  
27 moving mesh methods [? ? ? ? ? ] to address these complexities. Baines et al. introduced a moving mesh finite  
28 element method, where the mesh dynamically adjusts based on a local scale-invariant conservation principle [? ? ? ].  
29 Numerical experiments demonstrate a second-order convergence rate for this method when the mesh is appropriately  
30 selected initially. Duque et al. utilized a moving mesh partial differential equation (MMPDE) method to tackle the  
31 PME with a variable component  $m$  [? ? ]. Ngo & Huang [? ? ] also applied the MMPDE approach to solve  
32 both the PME and the transformed pressure equation. Their detailed study on the impact of the metric tensor in a  
33 novel implementation of the velocity equation revealed that Hessian-based adaptive meshes yield optimal second-  
34 order convergence. Theoretical analysis for the moving mesh methods is usually difficult due to a lack of a variational  
35 formulation.

36 The previously mentioned methods are based on an Eulerian framework, where the computational domain is  
37 in the physical domain. Recently, there has been a surge in the development of Lagrangian-type methods, where  
38 the problem is formulated within a reference domain. Liu and his collaborators have introduced several schemes  
39 based on the energy variational method [? ? ? ]. Their research highlighted that specific selections of the energy  
40 and dissipation functionals can significantly enhance the efficiency of the numerical method. Furthermore, optimal  
41 error estimates have been established under certain regularity assumptions [? ]. Additionally, Carrillo et al. have  
42 devised a Lagrangian-type scheme [? ] and a particle method [? ] utilizing the theory of Wasserstein gradient flow.  
43 One challenge with Lagrangian-type methods is to solve some highly nonlinear problems at each time step. Proper  
44 iterative solver has to be chosen to solve the problem efficiently.

45 In this paper, our objective is to devise a numerical method for the PME that combines the strengths of both the  
46 conventional moving mesh method (e.g. in an Eulerian framework) and Lagrangian-type methods (e.g. based on  
47 a variational formulation). To achieve this goal, we will leverage the Onsager principle as an approximation tool.  
48 The Onsager variational principle is a fundamental law for characterizing irreversible processes in nonequilibrium  
49 thermodynamics [? ? ]. This principle has been instrumental in deriving mathematical models for various soft matter  
50 physics problems [? ]. Recent studies have demonstrated the effectiveness of the Onsager principle as a powerful  
51 approximation tool for deriving reduced models (c.f. [? ? ? ? ? ], among others). Moreover, the Onsager principle  
52 has been utilized in designing numerical schemes [? ? ]. It has also been shown that the moving finite element method  
53 can be naturally derived from this principle [? ].

54 Motivated by the previous studies, we derive a novel numerical method for the PME in this paper. We first  
55 demonstrate the natural derivation of the PME from the Onsager principle. We treat the continuum equation  $\partial_t \rho +$   
56  $\nabla \cdot (\rho v) = 0$  as a constraint and incorporate a Lagrange multiplier into the Reyleignian functional to obtain a mixed  
57 version of the PME. Subsequently, we approximate the unknown function  $\rho$  and the multiplier by finite element  
58 functions on a triangulation with movable nodes. These nodes are assumed to move at the same velocity as dictated  
59 by the continuum equation. By reapplying the Onsager principle, we formulate a semi-discrete numerical scheme in  
60 mixed form, demonstrating that the scheme upholds the same energy dissipation relation as the continuous problem.

61 When employing an explicit time derivative discretization, a decoupled numerical scheme emerges, where a few  
62 linear equations are sequentially solved at each time step. We also develop an implicit scheme which leads to the  
63 establishment of the energy dissipation relation for the fully discrete method. We also explore the impact of the  
64 mass conservation property by varying the boundary condition for the Lagrange multiplier. Numerical examples  
65 show that our methods exhibit optimal convergence rates and accurately capture the waiting time phenomenon in both  
66 one-dimensional and two-dimensional scenarios.

67 The rest of the paper is organized as follows. In Section 2, we present the derivation of the PME by using the  
68 Onsager variational principle. We then apply the Onsager principle in the finite element space to derive two numerical  
69 schemes in Section 3. In Section 4, we discuss briefly an alternative semi-discrete scheme with improved mass  
70 conservation property. Numerical examples are given in Section 5 to illustrate the efficiency of our methods. A few  
71 concluding remarks are given in the last section.

## 72 2. Derivation of the PME by the Onsager principle

73 In this section, we will derive a model for gas flow in a homogeneous porous medium by the Onsager variational  
74 principle[? ? ]. For simplicity, we consider the dimensionless model throughout the paper. We denote by  $\rho(x, t)$  the  
75 mass density of a gas in a porous medium. Suppose the free energy is given by [? ]

$$\mathcal{E}(\rho) = \int_{\Omega(t)} f(\rho(x, t)) dx, \quad (2)$$

76 where  $\Omega(t) \subset \mathbb{R}^d$  is the domain where the gas flow occupies at time  $t$ , and  $f(\rho) = \frac{1}{m-1}\rho^m (m > 1)$  is the free energy  
77 density. From thermodynamic theory, the gas pressure is  $p = \delta\mathcal{E}/\delta\rho = f'(\rho)$ . Let the vector field  $v(x, t) : \Omega \times [0, T] \mapsto$   
78  $\mathbb{R}^n$  be the average velocity of the gas. Denote by  $J = \rho v$  the mass flux in the system. Then we have the mass  
79 conservation equation,

$$\partial_t \rho + \nabla \cdot J = 0. \quad (3)$$

80 In this setting, the mass flux through the boundary  $\partial\Omega$  is zero, i.e.,  $J \cdot n|_{\partial\Omega} = 0$ , where  $n$  is the outward unit normal on  
81 the boundary.

82 To derive the PME by the Onsager principle, we first calculate the changing rate of the free energy. By Reynold's  
83 transport theorem, we obtain

$$\dot{\mathcal{E}} = \frac{d}{dt} \int_{\Omega(t)} f(\rho) dx = \int_{\Omega(t)} f'(\rho) \partial_t \rho dx + \int_{\partial\Omega(t)} f(\rho) v \cdot n ds = \int_{\Omega(t)} f'(\rho) \partial_t \rho dx, \quad (4)$$

84 where the last equality uses the zero mass flux condition on the boundary. Then we define the dissipation function as

$$\Phi(\rho; v) = \int_{\Omega(t)} \frac{1}{2} \rho |v|^2 dx. \quad (5)$$

85 The Rayleighian functional is given by

$$\mathcal{R} = \Phi + \dot{\mathcal{E}}. \quad (6)$$

86 There are two ways to derive the PME by the Onsager variational principle. In the first approach, we derive the  
87 PME by minimizing the Rayleighian functional with respect to the mass flux  $J$ . Direct calculate give

$$\begin{aligned} \mathcal{R} &= \int_{\Omega(t)} \frac{|J|^2}{2\rho} dx + \int_{\Omega(t)} f'(\rho) \partial_t \rho dx = \int_{\Omega(t)} \frac{|J|^2}{2\rho} dx - \int_{\Omega(t)} f'(\rho) \nabla \cdot J dx \\ &= \int_{\Omega(t)} \frac{|J|^2}{2\rho} dx + \int_{\Omega(t)} \nabla f'(\rho) J dx, \end{aligned} \quad (7)$$

where the second equation utilizes the continuity equation (3) and the last equation utilizes the integration by parts.  
We minimize  $\mathcal{R}$  with respect to the flux  $J$ , i.e.

$$\min_J \mathcal{R}(J).$$

88 The corresponding Euler-Langrange equation is

$$J = -\rho \nabla f'(\rho) = -\nabla \rho^m. \quad (8)$$

89 Substituting the equation into (3), we have the PME

$$\partial_t \rho = \Delta \rho^m. \quad (9)$$

90 Although the above derivation is straightforward, we will present a different approach below, which is more helpful  
 91 to propose a numerical method. We will derive the PME by minimizing the Rayleighian functional with respect to  $\partial_t \rho$   
 92 and  $v$  under the constraint of the mass conservation equation. That is to consider the problem

$$\begin{aligned} \min_{\partial_t \rho, v} \mathcal{R}(\rho; \partial_t \rho, v) &= \Phi(\rho; v) + \dot{\mathcal{E}}(\rho; \partial_t \rho) = \frac{1}{2} \int_{\Omega(t)} \rho |v|^2 dx + \int_{\Omega(t)} f'(\rho) \partial_t \rho dx, \\ \text{s.t. } \partial_t \rho + \nabla \cdot (\rho v) &= 0. \end{aligned} \quad (10)$$

93 By introducing a Lagrange multiplier  $\lambda(x)$ , we obtain a Lagrangian functional

$$\tilde{\mathcal{R}} = \frac{1}{2} \int_{\Omega(t)} \rho |v|^2 dx + \int_{\Omega(t)} f'(\rho) \partial_t \rho dx - \int_{\Omega(t)} \lambda(x) (\partial_t \rho + \nabla \cdot (\rho v)) dx. \quad (11)$$

94 The corresponding Euler-Lagrange equation is

$$\begin{cases} f'(\rho) - \lambda(x) = 0, \\ v + \nabla \lambda = 0, \\ \partial_t \rho + \nabla \cdot (\rho v) = 0. \end{cases} \quad (12)$$

95 In the above equation, the Lagrange multiplier  $\lambda(x)$  has a physical interpretation that  $\lambda = f'(\rho) = \frac{m}{m-1} \rho^{m-1}$  is the  
 96 pressure. Since  $m > 1$ , we have  $\lambda = 0$  on  $\partial \Omega$ . The property is important for us to derive a decoupled scheme in the  
 97 next section. Note that  $v = -\nabla \lambda$  is the Darcy's law. By the above equation, we can easily derive the PME (9). The  
 98 equation (12) can be seen as a mixed form of the equation (9).

99 It is easy to see that the solution  $\rho$  of the equation (12) satisfies the following energy decay property

$$\frac{d\mathcal{E}}{dt} \leq 0. \quad (13)$$

100 Actually, by using the property  $\rho \geq 0$ , we have

$$\begin{aligned} \frac{d\mathcal{E}}{dt} &= \int_{\Omega(t)} f'(\rho) \partial_t \rho dx = \int_{\Omega(t)} \nabla f'(\rho) \cdot \rho v dx = \int_{\Omega(t)} \nabla \lambda \cdot \rho v dx \\ &= - \int_{\Omega(t)} \rho |v|^2 dx = -2\Phi(\rho; v) \leq 0. \end{aligned} \quad (14)$$

101 In the previous derivation, we see that  $v = -\nabla \lambda$  may not be equal to zero on  $\partial \Omega$ . This implies that the PME is a  
 102 free boundary problem. We rewrite the equation in a closed form that

$$\begin{cases} \partial_t \rho = \Delta \rho^m, & \text{in } \Omega(t), \\ \rho = 0, & \text{on } \partial \Omega(t), \\ v_n = -\frac{m}{m-1} \nabla \rho^{m-1} \cdot n, & \text{on } \partial \Omega(t), \\ \rho(x, 0) = \rho_0(x), & \text{at } t = 0. \end{cases} \quad (15)$$

103 where  $v_n = v \cdot n$  is the outer normal velocity of the free boundary. The well-posedness of the equation can be found in  
 104 [? ]. In addition to the mass conservation and energy decay properties, the PME has some other interesting properties,  
 105 like the waiting time phenomenon and the finite diffusion velocity, etc. In next section, we will derive a numerical  
 106 method to the PME by using the Onsager principle as an approximation tool.

### 107 3. A moving mesh finite element method

108 For simplicity in presentation, we derive a moving mesh finite element method by using the Onsager variational  
 109 principle in one dimension in this section. The derivation can be generalized to higher dimensional cases straightfor-  
 110 wardly (c.f. the two dimensional cases in the appendix). Let the interval  $I(t) = [a(t), b(t)]$  be the domain where the  
 111 PME is defined. The equation (15) is reduced to

$$\begin{cases} \partial_t \rho(x, t) = \partial_{xx} \rho^m(x, t), & x \in I(t), t > 0, \\ \rho(a(t), t) = 0, \quad \rho(b(t), t) = 0, & t > 0, \\ \dot{a} = -\frac{m}{m-1} \partial_x \rho^{m-1}(a), \quad \dot{b} = -\frac{m}{m-1} \partial_x \rho^{m-1}(b), & t > 0, \\ \rho(x, 0) = \rho^0(x), & x \in I(0). \end{cases} \quad (16)$$

112 We will not directly discretize the problem (16). Instead we derive a discrete problem by the Onsager variational  
 113 principle.

#### 114 3.1. Semi-discretization

115 We first partition the interval  $I(t)$  by  $N + 1$  knots,

$$X(t) := \{a(t) = x_0(t) < x_1(t) < \cdots < x_N(t) = b(t)\}. \quad (17)$$

116 Notice that the knots may change positions with respect to time. Denote the partition as  $\mathcal{T}_h := \{I_i\}_{i=1}^N$ , where  $I_i =$   
 117  $(x_{i-1}(t), x_i(t)]$ . Then we can define the finite element space  $V_h^t$

$$V_h^t := \{u_h \in C(I(t)) : u_h \text{ is linear in } I_i(t), \forall i = 1, \dots, N\}. \quad (18)$$

118 Denote by  $V_{h,0}^t = \{u_h \in V_h^t : u_h(a) = u_h(b) = 0\}$ . For any function  $\rho_h(x, t) \in V_{h,0}^t$ , it can be written as

$$\rho_h(x, t) = \sum_{i=1}^{N-1} \rho_i(t) \phi_i(x, t), \quad (19)$$

119 where  $\phi_i(x, t)$  is the finite element basis function associated with  $x_i$ , i.e.

$$\phi_i(x, t) = \phi_i^l + \phi_i^r = \frac{x - x_{i-1}(t)}{x_i(t) - x_{i-1}(t)} \chi_{I_i}(x) + \frac{x_{i+1}(t) - x}{x_{i+1}(t) - x_i(t)} \chi_{I_{i+1}}(x), \quad (20)$$

120 where  $\chi_{I_i}$  is the characteristic function corresponding to  $I_i$ . Due to the Dirichlet boundary condition  $\rho_0(t) = \rho_N(t) = 0$ ,  
 121 there are  $2N$  time dependent parameters in the formula of  $\rho_h(t, x)$ , i.e.,

$$\{\rho_1(t), \rho_2(t), \dots, \rho_{N-1}(t), x_0(t), x_1(t), \dots, x_N(t)\}. \quad (21)$$

122 We aim to approximate the solution  $\rho$  of the problem (16) by a discrete function  $\rho_h(t, x)$ . For that propose, we will  
 123 derive a dynamic equation for  $\rho_i(t)$  and  $x_i(t)$  by using the Onsager principle.

Firstly, we discretize the energy functional and as follows. Notice that the time derivative and space derivative of  $\rho_h(t, x)$  are respectively given by

$$\begin{aligned} \partial_t \rho_h &= \sum_{i=1}^{N-1} \dot{\rho}_i(t) \phi_i(x, t) + \sum_{i=0}^N \dot{x}_i(t) \psi_i(x, t), \\ \partial_x \rho_h &= \sum_{i=1}^{N-1} \rho_i(t) \partial_x \phi_i(x, t), \end{aligned}$$

where

$$\psi_i(x, t) = \frac{\partial \rho_h}{\partial x_i} = -D_h \rho_{i-1} \phi_i^l - D_h \rho_i \phi_i^r,$$

124 with  $D_h \rho_i = \frac{\rho_{i+1}(t) - \rho_i(t)}{x_{i+1}(t) - x_i(t)}$ .

125 Denote by  $\boldsymbol{\rho} = (\rho_1(t), \dots, \rho_{N-1}(t))^T$ ,  $\mathbf{x} = (x_0(t), \dots, x_N(t))^T$ . The discrete energy functional  $\mathcal{E}_h$  with respect to  $\rho_h$  is  
 126 given by

$$\mathcal{E}_h(\boldsymbol{\rho}, \mathbf{x}) = \sum_{i=1}^N \int_{I_i} f(\rho_h) dx. \quad (22)$$

127 Then the changing rate of the discrete energy is calculated as

$$\dot{\mathcal{E}}_h(\boldsymbol{\rho}, \mathbf{x}; \dot{\boldsymbol{\rho}}, \dot{\mathbf{x}}) = \sum_{i=1}^{N-1} \frac{\partial \mathcal{E}_h}{\partial \rho_i} \dot{\rho}_i + \sum_{i=0}^N \frac{\partial \mathcal{E}_h}{\partial x_i} \dot{x}_i, \quad (23)$$

where

$$\begin{aligned} \frac{\partial \mathcal{E}_h}{\partial \rho_i} &= \int_I f'(\rho_h) \phi_i dx, \quad i = 1, \dots, N-1; \\ \frac{\partial \mathcal{E}_h}{\partial x_i} &= \int_I f'(\rho_h) \psi_i dx, \quad i = 0, \dots, N. \end{aligned}$$

128 In order to obtain the discrete dissipation functional, we need to discretize the velocity  $v(x, t)$ . We use a piecewise  
 129 linear function  $v_h(x, t) = \sum_{i=0}^N v_i(t) \phi_i(x, t)$  in  $V_h^t$  to approximate the velocity  $v(x, t)$ . Denote by  $\mathbf{v} = (v_0(t), \dots, v_N(t))^T$ .  
 130 Then we calculate the discrete dissipation function  $\Phi_h$  as

$$\Phi_h(\boldsymbol{\rho}, \mathbf{x}; \mathbf{v}) = \sum_{i=1}^N \int_{I_i} \frac{1}{2} \rho_h(x, t) v_h(x, t)^2 dx. \quad (24)$$

131 Suppose that the mesh knots move with velocity  $v_h$  in a Lagrange manner, i.e.

$$\dot{x}_i(t) = v_h(x_i, t), \quad i = 0, \dots, N. \quad (25)$$

132 Then the time derivative of  $\mathcal{E}_h$  can be rewritten as

$$\dot{\mathcal{E}}_h(\boldsymbol{\rho}, \mathbf{x}; \dot{\boldsymbol{\rho}}, \mathbf{v}) = \sum_{i=1}^{N-1} \frac{\partial \mathcal{E}_h}{\partial \rho_i} \dot{\rho}_i + \sum_{i=0}^N \frac{\partial \mathcal{E}_h}{\partial x_i} v_i. \quad (26)$$

The discrete Rayleighian functional is defined as

$$\mathcal{R}_h(\boldsymbol{\rho}, \mathbf{x}; \dot{\boldsymbol{\rho}}, \mathbf{v}) = \Phi_h(\boldsymbol{\rho}; \mathbf{x}, \mathbf{v}) + \dot{\mathcal{E}}_h(\boldsymbol{\rho}, \mathbf{x}; \dot{\boldsymbol{\rho}}, \mathbf{v}).$$

133 By the Onsager variational principle,  $(\dot{\boldsymbol{\rho}}, \mathbf{v})$  is obtained by

$$\begin{aligned} &\min_{\dot{\boldsymbol{\rho}}, \mathbf{v}} \mathcal{R}_h(\boldsymbol{\rho}, \mathbf{x}; \dot{\boldsymbol{\rho}}, \mathbf{v}) \\ &s.t. \quad \int_I (\partial_t \rho_h + \partial_x(\rho_h v_h)) w_h dx = 0, \quad \forall w_h \in V_{h,0}^t. \end{aligned} \quad (27)$$

To deal with the constraint in the above problem, we introduce a discrete Lagrange multiplier  $\lambda_h = \sum_{i=1}^{N-1} \lambda_i \phi_i(x, t)$ .  
 By integration by part, we have

$$\int_I (\partial_t \rho_h + \partial_x(\rho_h v_h)) \lambda_h dx = \int_I (\partial_t \rho_h \lambda_h - \rho_h v_h \partial_x \lambda_h) dx.$$

134 Then the discrete Lagrangian functional is given by

$$\tilde{\mathcal{R}}_h = \Phi_h + \dot{\mathcal{E}}_h - \int_I (\partial_t \rho_h \lambda_h - \rho_h v_h \partial_x \lambda_h) dx. \quad (28)$$

135 Notice that the problem can be seen as a discrete version of the equation (10). Here we consider a weak form of the  
 136 continuum equation in the constraint. Notice that the test function is chosen to be in a finite element space  $V_{h,0}^t$  instead  
 137 of  $V_h^t$ . This will lead to a discrete multiplier  $\lambda_h \in V_{h,0}^t$  in the Euler-Lagrange equation. This is consistent with the  
 138 continuous problem where the multiplier (pressure)  $\lambda = 0$  on  $\partial\Omega$ .

139 The Euler-Lagrange equation corresponding to the problem (28) is given by

$$\begin{cases} \frac{\partial \mathcal{E}_h}{\partial \rho_i} - \int_I \phi_i \lambda_h dx = 0, & i = 1, \dots, N-1; \\ \int_I \rho_h v_h \phi_i dx + \frac{\partial \mathcal{E}_h}{\partial x_i} - \int_I \psi_i \lambda_h dx + \int_I \rho_h \partial_x \lambda_h \phi_i dx = 0, & i = 0, \dots, N; \\ \int_I \partial_t \rho_h \phi_i dx - \int_I \rho_h v_h \partial_x \phi_i dx = 0, & i = 1, \dots, N-1. \end{cases} \quad (29)$$

140 Notice that  $\dot{\mathbf{x}} = \mathbf{v}$ , the equations (29) can be written in an algebraic form

$$\begin{cases} \mathbf{M}(\mathbf{x}(t))\lambda(t) = \frac{\partial \mathcal{E}_h}{\partial \rho}(\mathbf{x}(t), \boldsymbol{\rho}(t)), \\ \mathbf{D}(\mathbf{x}(t), \boldsymbol{\rho}(t))\dot{\mathbf{x}}(t) = -\frac{\partial \mathcal{E}_h}{\partial \mathbf{x}}(\mathbf{x}(t), \boldsymbol{\rho}(t)) + (\mathbf{B}^T(\mathbf{x}(t)) - \mathbf{E}^T(\mathbf{x}(t), \boldsymbol{\rho}(t)))\lambda(t), \\ \mathbf{M}(\mathbf{x}(t))\dot{\boldsymbol{\rho}}(t) + (\mathbf{B}(\mathbf{x}(t)) - \mathbf{E}(\mathbf{x}(t), \boldsymbol{\rho}(t)))\dot{\mathbf{x}}(t) = 0, \end{cases} \quad (30)$$

where  $\mathbf{M} \in \mathbb{R}^{N-1, N-1}$ ,  $\mathbf{D} \in \mathbb{R}^{N+1, N+1}$ ,  $\mathbf{B} \in \mathbb{R}^{N-1, N+1}$ ,  $\mathbf{E} \in \mathbb{R}^{N-1, N+1}$ , such that

$$\begin{aligned} M_{ij}(\mathbf{x}(t)) &= \int_{I(t)} \phi_i \phi_j dx; & D_{ij}(\mathbf{x}(t), \boldsymbol{\rho}(t)) &= \int_{I(t)} \rho_h \phi_i \phi_j dx; \\ B_{ij}(\mathbf{x}(t)) &= \int_{I(t)} \phi_i \psi_j dx; & E_{ij}(\mathbf{x}(t), \boldsymbol{\rho}(t)) &= \int_{I(t)} \rho_h \partial_x \phi_i \phi_j dx. \end{aligned}$$

141 In the following of the subsection, we give some important properties for the differential-algebraic system (30).  
 142 We first address the existence of solutions  $\boldsymbol{\rho}(t)$  and  $\mathbf{x}(t)$  with non-negative initial data  $\boldsymbol{\rho}_0$  and an initial partition  $\mathbf{x}_0$ .  
 143 We need some assumptions:

144 **(A1).** The intervals  $I_i(t)$ ,  $i = 1, \dots, N$  are well-defined, i.e.,  $x_{i-1}(t) < x_i(t)$ .

145 **(A2).** The discrete density function  $\boldsymbol{\rho}(t)$  is non-negative for all  $t$ .

146 **Proposition 1.** *Under the assumptions (A1) and (A2), there exist a unique solution for differential-algebraic system*  
 147 *(29).*

*Proof.* By the assumption (A1), the mass matrix  $\mathbf{M}(\mathbf{x}(t))$  is positive definite for any  $t$ . Then  $\lambda(t)$  can be solved in the algebraic equation, i.e.  $\lambda = \mathbf{M}^{-1} \frac{\partial \mathcal{E}_h}{\partial \rho}$ . By the assumption (A2), the matrix  $\mathbf{D}(\mathbf{x}, \boldsymbol{\rho})$  is also positive definite. Then the differential-algebraic system reduces to a system of ordinary differential equations (ODEs)

$$\begin{cases} \dot{\mathbf{x}}(t) = -g_1(\mathbf{x}(t), \boldsymbol{\rho}(t)), \\ \dot{\boldsymbol{\rho}}(t) = g_2(\mathbf{x}(t), \boldsymbol{\rho}(t))g_1(\mathbf{x}(t), \boldsymbol{\rho}(t)), \end{cases}$$

where

$$\begin{aligned} g_1(\mathbf{x}(t), \boldsymbol{\rho}(t)) &= \mathbf{D}^{-1}(\mathbf{x}(t), \boldsymbol{\rho}(t)) \left[ \frac{\partial \mathcal{E}_h}{\partial \mathbf{x}}(\mathbf{x}(t), \boldsymbol{\rho}(t)) - (\mathbf{B}^T(\mathbf{x}(t)) - \mathbf{E}^T(\mathbf{x}(t), \boldsymbol{\rho}(t)))\lambda(t) \right], \\ g_2(\mathbf{x}(t), \boldsymbol{\rho}(t)) &= \mathbf{M}^{-1}(\mathbf{x}(t)) (\mathbf{B}(\mathbf{x}(t)) - \mathbf{E}(\mathbf{x}(t), \boldsymbol{\rho}(t))). \end{aligned}$$

148 It is easy to verify that the vector-valued functions  $g_1(\mathbf{x}, \boldsymbol{\rho})$  and  $g_2(\mathbf{x}, \boldsymbol{\rho})$  have continuous partial derivatives with respect  
 149 to  $\boldsymbol{\rho}$  and  $\mathbf{x}$  on a bounded closed convex domain by direct calculations. Therefore they are Lipschitz continuous with  
 150 respect to  $(\mathbf{x}(t), \boldsymbol{\rho}(t))$ . By the Picard-Lindelof theorem, we know that the ODE system has a unique solution for given  
 151 proper initial values.  $\square$

152 The following theorem states the discrete energy dissipation relations.

153 **Theorem 1.** Under the assumptions (A1) and (A2), and let  $\rho(t), \mathbf{x}(t)$  be the solution of the equations (25) and (29).  
 154 Let  $\rho_h(t, x) \in V_{h,0}^t$  be the corresponding discrete density function and  $v_h \in V_h^t$  be the discrete velocity function. Then  
 155 we have

$$\frac{\partial \mathcal{E}_h(\rho_h)}{\partial t} = -2\Phi_h(\rho_h, v_h) \leq 0. \quad (31)$$

*Proof.* The proof is given by straightforward calculations

$$\begin{aligned} \frac{\partial \mathcal{E}_h(\rho_h)}{\partial t} &= \sum_{i=1}^{N-1} \frac{\partial \mathcal{E}_h}{\partial \rho_i} \dot{\rho}_i + \sum_{i=0}^N \frac{\partial \mathcal{E}_h}{\partial x_i} \dot{x}_i \\ &= \sum_{i=1}^{N-1} \int_I \phi_i \lambda_h dx \dot{\rho}_i + \sum_{i=0}^N \left( - \int_I \rho_h \partial_x \lambda_h \phi_i dx - \int_I \rho_h v_h \phi_i dx + \int_I \psi_i \lambda_h dx \right) v_i \\ &= \sum_{i=1}^{N-1} \left( \int_I \partial_t \rho_h \phi_i dx - \int_I \rho_h v_h \partial_x \phi_i dx \right) \lambda_i - \sum_{i=0}^N \int_I \rho_h v_h \phi_i dx v_i \\ &= - \int_I \rho_h v_h^2 dx = -2\Phi_h(\rho_h, v_h). \end{aligned}$$

By the assumption (A2), the function  $\rho_h(x, t) \geq 0$  for all  $x \in I(t)$ . Then we can easily see that

$$\int_I \rho_h v_h^2 dx \geq 0.$$

156 This leads to the proof of the theorem. □

157 Finally, we show a property of the semi-discrete problem which is related to the mass conservation.

158 **Proposition 2.** Under the assumptions (A1) and (A2), and let  $\rho(t), \mathbf{x}(t)$  be the solution of the equations (25) and (29).  
 159 We have the following relations,

$$\frac{d}{dt} \int_{I(t)} \rho_h(x, t) \phi_i(x, t) dx = 0, \quad i = 1, \dots, N-1. \quad (32)$$

*Proof.* Using integration by parts, we can obtain

$$\begin{aligned} &\frac{d}{dt} \int_{I(t)} \rho_h(x, t) \phi_i(x, t) dx \\ &= \int_{I(t) \cup I_{i+1}(t)} (\partial_t \rho_h + \partial_x(\rho_h v_h)) \phi_i + \rho_h (\partial_t \phi_i + v_h \partial_x \phi_i) dx. \end{aligned}$$

Notice that

$$\partial_t \phi_i = \sum_{j=i-1}^{i+1} \partial_{x_j} \phi_i \dot{x}_j = \sum_{j=i-1}^{i+1} (-\phi_j \partial_x \phi_i) \dot{x}_j = - \left( \sum_{j=i-1}^{i+1} \phi_j \dot{x}_j \right) \partial_x \phi_i = -v_h \partial_x \phi_i.$$

This leads to  $\partial_t \phi_i + v_h \partial_x \phi_i = 0$ . Thus by (29) we have

$$\frac{d}{dt} \int_{I(t)} \rho_h(x, t) \phi_i(x, t) dx = 0, \quad i = 1, \dots, N-1.$$

160 □

**Remark 1.** We can rewrite the equations (32) in a vector form

$$\frac{d}{dt} (\mathbf{M}(t) \boldsymbol{\rho}(t)) = 0,$$



161 Integrating the equation from 0 to  $T$ , we have  $\mathbf{M}(T)\boldsymbol{\rho}(T) = \mathbf{M}(0)\boldsymbol{\rho}(0)$ . Notice that this does not imply the exact mass  
 162 conservation property. We will give more discussions on this issue in the next section. In addition, given a discrete  
 163 initial value  $\boldsymbol{\rho}(0)$ , it is easy to show  $\mathbf{M}(0)\boldsymbol{\rho}(0) \geq 0$ . However, since the mass matrix  $\mathbf{M}(T)$  is not a  $M$ -matrix in  
 164 general, we can not prove the positivity of  $\boldsymbol{\rho}(T)$ . That is why we need the assumption (A2). To ensure the positivity  
 165 of the mass density, we can use the lumped mass method [? ]. The matrix  $\mathbf{M}(t)$  in the equation (30) is replaced by a  
 166 diagonal matrix  $\bar{\mathbf{M}}(t)$ . A diagonal element of  $\bar{\mathbf{M}}(t)$  is the sum of the nonzero elements of  $\mathbf{M}(t)$  on the corresponding  
 167 row. One can easily verify that  $\bar{\mathbf{M}}(t)$  is a  $M$ -matrix and the positivity of  $\rho$  is guaranteed. In Section 5, we will show  
 168 some numerical tests using the lumped mass method.

### 169 3.2. Full discretization

170 In order to get a fully discrete numerical scheme, we introduce a proper temporal discretization to the semi-discrete  
 171 equations (25) and (29). Let the time step be  $\tau$ , then we set the solution at  $t = t^n$  as  $\rho_i^n = \rho_i(t^n)$ ,  $x_i^n = x_i(t^n)$ , and the  
 172 solution at  $t^{n+1}$  as  $\rho_i^{n+1}$ ,  $x_i^{n+1}$ . We define the finite difference operator  $\bar{\partial}\rho^n = (\rho^{n+1} - \rho^n)/\tau$ , then let  $v_i^{n+1} := \bar{\partial}x_i^n =$   
 173  $(x_i^{n+1} - x_i^n)/\tau$ . We first consider an explicit Euler scheme as follows

$$\int_{I^n} \phi_i^n \lambda_h^{n+1} dx = \frac{\partial \mathcal{E}_h^n}{\partial \rho_i^n}, \quad i = 1, \dots, N-1; \quad (33)$$

$$\int_{I^n} \rho_h^n v_h^{n+1} \phi_i^n dx = -\frac{\partial \mathcal{E}_h^n}{\partial x_i^n} + \int_{I^n} \psi_i^n \lambda_h^{n+1} dx - \int_{I^n} \rho_h^n \partial_x \lambda_h^{n+1} \phi_i^n dx, \quad i = 0, \dots, N; \quad (34)$$

$$\int_{I^n} \left( \sum_{j=1}^{N-1} \bar{\partial} \rho_j^n \phi_j^n \right) \phi_i^n = - \int_{I^n} \left( \sum_{j=0}^N v_j^{n+1} \psi_j^n \right) \phi_i^n dx + \int_{I^n} \rho_h^n v_h^{n+1} \partial_x \phi_i^n dx, \quad i = 1, \dots, N-1. \quad (35)$$

The above scheme is decoupled and easy to implement. We need only to solve a few linear equation successively in each time step. This is efficient in general case. A drawback of the scheme is that we show choose a small time step  $\tau$  to guarantee numerical stability. To further improve the stability of the explicit scheme, we add some stabilization terms by incorporating the Hessian matrix of the energy. This results in a coupled stabilized explicit scheme as follows,

$$\int_{I^n} \phi_i^n \lambda_h^{n+1} dx - \tau \frac{\partial^2 \mathcal{E}_h^n}{\partial \rho_i^n \partial x_i^n} \bar{\partial} x_i^n - \tau \frac{\partial^2 \mathcal{E}_h^n}{\partial \rho_i^n \partial \rho_i^n} \bar{\partial} \rho_i^n = \frac{\partial \mathcal{E}_h^n}{\partial \rho_i^n}, \quad i = 1, \dots, N-1; \quad (36)$$

$$\int_{I^n} \rho_h^n v_h^{n+1} \phi_i^n dx + \tau \frac{\partial^2 \mathcal{E}_h^n}{\partial x_i^n \partial \rho_i^n} \bar{\partial} \rho_j^n + \tau \frac{\partial^2 \mathcal{E}_h^n}{\partial x_i^n \partial x_i^n} \bar{\partial} x_i^n - \int_{I^n} \psi_i^n \lambda_h^{n+1} dx + \int_{I^n} \rho_h^n \partial_x \lambda_h^{n+1} \phi_i^n dx = -\frac{\partial \mathcal{E}_h^n}{\partial x_i^n}, \quad i = 0, \dots, N; \quad (37)$$

$$\int_{I^n} \left( \sum_{j=1}^{N-1} \bar{\partial} \rho_j^n \phi_j^n \right) \phi_i^n + \int_{I^n} \left( \sum_{j=0}^N v_j^{n+1} \psi_j^n \right) \phi_i^n dx - \int_{I^n} \rho_h^n v_h^{n+1} \partial_x \phi_i^n dx = 0, \quad i = 1, \dots, N-1. \quad (38)$$

174

Another approach is to adopt an implicit numerical scheme for the temporal discretization as follows,

$$\int_{I^n} \phi_i^n \lambda_h^{n+1} dx = \frac{\partial \mathcal{E}_h^{n+1}}{\partial \rho_i^{n+1}}, \quad i = 1, \dots, N-1; \quad (39)$$

$$\int_{I^n} \rho_h^n v_h^{n+1} \phi_i^n dx = -\frac{\partial \mathcal{E}_h^n}{\partial x_i^n} + \int_{I^n} \psi_i^n \lambda_h^{n+1} dx - \int_{I^n} \rho_h^n \partial_x \lambda_h^{n+1} \phi_i^n dx, \quad i = 0, \dots, N; \quad (40)$$

$$\int_{I^n} \left( \sum_{j=1}^{N-1} \bar{\partial} \rho_j^n \phi_j^n \right) \phi_i^n = - \int_{I^n} \left( \sum_{j=0}^N v_j^{n+1} \psi_j^n \right) \phi_i^n dx + \int_{I^n} \rho_h^n v_h^{n+1} \partial_x \phi_i^n dx, \quad i = 1, \dots, N-1. \quad (41)$$

175 In the following theorem, we prove the energy stability of the implicit scheme.

176 **Theorem 2.** Let  $\rho_i^n, x_i^n$  and  $\rho_i^{n+1}, x_i^{n+1}$  be the solutions of the equations (39)-(41) at  $t = t^n$  and  $t = t^{n+1}$ , respectively.  
 177 We have the following result:

$$\mathcal{E}_h(\boldsymbol{\rho}^{n+1}, \mathbf{x}^{n+1}) \leq \mathcal{E}_h(\boldsymbol{\rho}^n, \mathbf{x}^n). \quad (42)$$

*Proof.* Denote by  $r_i^n(s) = x_{i-1}^n + s(x_i^n - x_{i-1}^n)$ ,  $\rho_h \circ r_i^n = \rho_{i-1}^n + s(\rho_i^n - \rho_{i-1}^n)$ . And let  $w_1 = \rho_h^{n+1} \circ r_i^{n+1}$  and  $w_2 = \rho_h^n \circ r_i^n$ . Since function  $f$  is convex, we know that the energy  $\mathcal{E}(\rho)$  is a convex functional. Then we have the following property

$$\mathcal{E}(w_1) - \mathcal{E}(w_2) \leq \left\langle \frac{\delta \mathcal{E}(w_1)}{\delta w_1}, w_1 - w_2 \right\rangle.$$

By direct calculation, we have

$$\begin{aligned} \mathcal{E}_h(\rho_h^{n+1}) - \mathcal{E}_h(\rho_h^n) &= \sum_{i=1}^N \left( \int_{I_i^{n+1}} f(\rho_h^{n+1}) dx - \int_{I_i^n} f(\rho_h^n) dx \right) \\ &= \sum_{i=1}^N \left( \int_0^1 f(\rho_h^{n+1} \circ r_i^{n+1}) |I_i^{n+1}| ds - \int_0^1 f(\rho_h^n \circ r_i^n) |I_i^n| ds \right) \\ &= \sum_{i=1}^N \left( \int_0^1 (f(\rho_h^{n+1} \circ r_i^{n+1}) - f(\rho_h^n \circ r_i^n)) |I_i^{n+1}| ds \right. \\ &\quad \left. + \int_0^1 f(\rho_h^n \circ r_i^n) (|I_i^{n+1}| - |I_i^n|) ds \right). \end{aligned}$$

By using the convexity of  $\mathcal{E}$ , we have

$$\int_0^1 f(\rho_h^{n+1} \circ r_i^{n+1}) - f(\rho_h^n \circ r_i^n) ds \leq \int_0^1 f'(\rho_h^{n+1} \circ r_i^{n+1}) (\rho_h^{n+1} \circ r_i^{n+1} - \rho_h^n \circ r_i^n) ds.$$

178 Then

$$\begin{aligned} \mathcal{E}_h(\rho_h^{n+1}) - \mathcal{E}_h(\rho_h^n) &\leq \sum_{i=1}^N \left( \int_0^1 f'(\rho_h^{n+1} \circ r_i^{n+1}) |I_i^{n+1}| (\rho_h^{n+1} \circ r_i^{n+1} - \rho_h^n \circ r_i^n) ds \right. \\ &\quad \left. + \int_0^1 f(\rho_h^n \circ r_i^n) (\bar{\partial} x_i^n - \bar{\partial} x_{i-1}^n) \tau ds \right). \end{aligned} \quad (43)$$

179 Notice the expression

$$\mathcal{E}_h(\rho_h^n) = \int_{I^n} f(\rho_h^n) dx = \sum_{i=1}^N \int_0^1 f(\rho_h^n \circ r_i^n) |I_i^n| ds. \quad (44)$$

From the first equality of the above equation, we know that

$$\frac{\partial \mathcal{E}_h^n}{\partial x_i^n} = \int_{I^n} f'(\rho_h^n) \psi_i^n dx.$$

From the second equality of (44) and noticing that  $\rho_h \circ r_i^n = \rho_{i-1}^n + s(\rho_i^n - \rho_{i-1}^n)$ , which does not depend on  $x_i^n$ , we obtain

$$\frac{\partial \mathcal{E}_h^n}{\partial x_i^n} = \int_0^1 f(\rho_h^n \circ r_i^n) |I_i^n| ds - \int_0^1 f(\rho_h^n \circ r_{i+1}^n) |I_{i+1}^n| ds.$$

Thus we have the formula of  $\frac{\partial \mathcal{E}_h^n}{\partial x_i^n}$ :

$$\frac{\partial \mathcal{E}_h^n}{\partial x_i^n} = \int_{I^n} f'(\rho_h^n) \psi_i^n dx = \int_0^1 f(\rho_h^n \circ r_i^n) |I_i^n| ds - \int_0^1 f(\rho_h^n \circ r_{i+1}^n) |I_{i+1}^n| ds.$$

Similarity, we have the formula of  $\frac{\partial \mathcal{E}_h^{n+1}}{\partial \rho_i^{n+1}}$ :

$$\begin{aligned} \frac{\partial \mathcal{E}_h^{n+1}}{\partial \rho_i^{n+1}} &= \int_{I^{n+1}} f'(\rho_h^{n+1}) \phi_i^{n+1} dx \\ &= \int_0^1 f'(\rho_h^{n+1} \circ r_i^{n+1}) |I_i^{n+1}| s ds + \int_0^1 f'(\rho_h^{n+1} \circ r_{i+1}^{n+1}) |I_{i+1}^{n+1}| (1-s) ds. \end{aligned}$$

Then we derive the expressions for  $\sum_{i=1}^{N-1} \frac{\partial \mathcal{E}_h^{n+1}}{\partial \rho_i^{n+1}} \bar{\partial} \rho_i^n$  and  $\sum_{i=0}^N \frac{\partial \mathcal{E}_h^n}{\partial x_i^n} \bar{\partial} x_i^n$  as

$$\begin{aligned} \sum_{i=1}^{N-1} \frac{\partial \mathcal{E}_h^{n+1}}{\partial \rho_i^{n+1}} \bar{\partial} \rho_i^n &= \sum_{i=1}^N \int_0^1 f'(\rho_h^{n+1} \circ r_i^{n+1}) |I_i^{n+1}| ((1-s) \bar{\partial} \rho_{i-1}^n + s \bar{\partial} \rho_i^n) ds \\ &= \frac{1}{\tau} \sum_{i=1}^N \int_0^1 f'(\rho_h^{n+1} \circ r_i^{n+1}) |I_i^{n+1}| (\rho_h^{n+1} \circ r_i^{n+1} - \rho_h^n \circ r_i^n) ds, \end{aligned}$$

and

$$\sum_{i=0}^N \frac{\partial \mathcal{E}_h^n}{\partial x_i^n} \bar{\partial} x_i^n = \sum_{i=1}^N \int_0^1 f(\rho_h^n \circ r_i^n) (\bar{\partial} x_i^n - \bar{\partial} x_{i-1}^n) ds,$$

respectively. By using these relations, the equation (43) is reduced to

$$\mathcal{E}_h(\rho_h^{n+1}) - \mathcal{E}_h(\rho_h^n) \leq \tau \sum_{i=1}^{N-1} \frac{\partial \mathcal{E}_h^{n+1}}{\partial \rho_i^{n+1}} \bar{\partial} \rho_i^n + \tau \sum_{i=0}^N \frac{\partial \mathcal{E}_h^n}{\partial x_i^n} \bar{\partial} x_i^n.$$

By using the equations (39)-(41), we can further calculate

$$\begin{aligned} &\tau \sum_{i=1}^{N-1} \frac{\partial \mathcal{E}_h^{n+1}}{\partial \rho_i^{n+1}} \bar{\partial} \rho_i^n + \tau \sum_{i=0}^N \frac{\partial \mathcal{E}_h^n}{\partial x_i^n} \bar{\partial} x_i^n \\ &= \tau \sum_{i=1}^{N-1} \left( \int_{I^n} \phi_i^n \lambda_h^{n+1} dx \right) \bar{\partial} \rho_i^n \\ &\quad + \tau \sum_{i=0}^N \left( \int_{I^n} \psi_i^n \lambda_h^{n+1} dx - \int_{I^n} \rho_h^n \partial_x \lambda_h^{n+1} \phi_i^n dx - \int_{I^n} \rho_h^n v_h^{n+1} \phi_i^n dx \right) \bar{\partial} x_i^n \\ &= \tau \sum_{i=1}^{N-1} \left( \int_{I^n} \left( \sum_{j=1}^{N-1} \bar{\partial} \rho_j^n \phi_j^n \right) \phi_i^n + \int_{I^n} \left( \sum_{j=0}^N v_j^{n+1} \psi_j^n \right) \phi_i^n dx - \int_{I^n} \rho_h^n v_h^{n+1} \partial_x \phi_i^n dx \right) \lambda_i^n \\ &\quad - \tau \sum_{i=0}^N \left( \int_{I^n} \rho_h^n v_h^{n+1} \phi_i^n dx \right) \bar{\partial} x_i^n = -\tau \int_{I^n} \rho_h^n (v_h^{n+1})^2 dx \leq 0. \end{aligned}$$

Thus we obtain the following result:

$$\mathcal{E}_h(\rho_h^{n+1}) - \mathcal{E}_h(\rho_h^n) \leq 0.$$

180

□

### 181 3.3. Implementations of the numerical schemes

The fully discrete explicit scheme (33)-(35) can be written as

$$\mathbf{M}^n \boldsymbol{\lambda}^{n+1} = \frac{\partial \mathcal{E}_h^n}{\partial \boldsymbol{\rho}^n}, \quad (45)$$

$$\mathbf{D}^n \mathbf{v}^{n+1} = -\frac{\partial \mathcal{E}_h^n}{\partial \mathbf{x}^n} + (\mathbf{B}^n - \mathbf{E}^n)^T \boldsymbol{\lambda}^{n+1}, \quad (46)$$

$$\mathbf{M}^n \bar{\partial} \boldsymbol{\rho}^n = -(\mathbf{B}^n - \mathbf{E}^n) \mathbf{v}^{n+1}, \quad (47)$$

where  $\mathbf{M}^n \in \mathbb{R}^{N-1, N-1}$ ,  $\mathbf{D}^n \in \mathbb{R}^{N+1, N+1}$ ,  $\mathbf{B}^n \in \mathbb{R}^{N-1, N+1}$ ,  $\mathbf{E}^n \in \mathbb{R}^{N-1, N+1}$ , such that

$$\begin{aligned} M_{ij}^n &= \int_{I^n} \phi_i^n \phi_j^n dx; & D_{ij}^n &= \int_{I^n} \rho_h^n \phi_i^n \phi_j^n dx; \\ B_{ij}^n &= \int_{I^n} \phi_i^n \psi_j^n dx; & E_{ij}^n &= \int_{I^n} \rho_h^n \partial_x \phi_i^n \phi_j^n dx. \end{aligned}$$

182 Since  $\mathbf{M}^n$  is the mass matrix and  $\mathbf{D}^n$  is a modified mass matrix, both of them are positive definite if the value  $\rho^n$   
 183 and  $\mathbf{x}^n$  satisfy Assumptions (A1) and (A2). In implementations, we can first solve (45) to compute  $\lambda^{n+1}$ . Then we  
 184 successively solve (46) to obtain  $\mathbf{v}^{n+1}$  and (47) to get  $\rho^{n+1}$ . Finally, we update  $\mathbf{x}^{n+1}$  by  $\mathbf{x}^{n+1} = \mathbf{x}^n + \tau \mathbf{v}^{n+1}$ . The linear  
 185 system (45)-(47) are decoupled and are easy to solve.

The implicit scheme (39)-(41) can be written as

$$\mathbf{M}^n \lambda^{n+1} - \frac{\partial \mathcal{E}_h^{n+1}}{\partial \rho^{n+1}} = 0, \quad (48)$$

$$\mathbf{D}^n \mathbf{v}^{n+1} - (\mathbf{B}^n - \mathbf{E}^n)^T \lambda^{n+1} = -\frac{\partial \mathcal{E}_h^n}{\partial \mathbf{x}^n}, \quad (49)$$

$$\mathbf{M}^n \bar{\rho}^n + (\mathbf{B}^n - \mathbf{E}^n) \mathbf{v}^{n+1} = 0. \quad (50)$$

186 Since the coupled system (48)-(50) is nonlinear, we can choose Newton method or fixed-point iteration to solve them.

187 **Remark 2.** *The derivation and the theoretical results in this section can be generalized to higher dimensional cases*  
 188 *straightforwardly. More details on the methods in the two dimensional case are given in the appendix. Numerical*  
 189 *examples in two dimension are given in the Section 5.*

#### 190 4. Modified numerical schemes

191 Notice that the conservation of the total mass of the semi-discrete scheme (30) in the previous section is not  
 192 guaranteed, as discussed in Remark 1. This is due to the fact that we assume the homogeneous boundary condition of  
 193 the Lagrange multiplier(or the pressure) on the free boundary, i.e.  $\lambda_0 = \lambda_N = 0$ . This condition is consistent with the  
 194 continuous problem(see the equation (12)). However, we need consider an alternative boundary condition to preserve  
 195 the mass conservation for the semi-discrete scheme.

196 We still use a piecewisely linear approximation for  $\rho$  and allow the grid nodes move in a Lagrange manner.  
 197 Namely, we let  $\rho_h = \sum_{i=1}^{N-1} \rho_i \phi_i$  and  $v_i = \dot{x}_i$  for  $i = 0, \dots, N$ . In comparison with the previous derivation, we do not  
 198 propose the boundary condition for the Lagrange multiplier and let  $\widehat{\lambda}_h = \sum_{i=0}^N \lambda_i \phi_i$ . Then the augmented Rayleighian  
 199 functional is defined as

$$\widehat{\mathcal{R}}_h = \Phi_h + \dot{\mathcal{E}}_h - \int_I (\partial_t \rho_h + \partial_x(\rho_h v_h)) \widehat{\lambda}_h dx. \quad (51)$$

200 This corresponding variational problem is

$$\begin{aligned} & \min_{\rho, \mathbf{v}} \mathcal{R}_h(\rho, \mathbf{x}; \dot{\rho}, \mathbf{v}) \\ & s.t. \quad \int_I (\partial_t \rho_h + \partial_x(\rho_h v_h)) w_h dx = 0, \quad \forall w_h \in V_h^t. \end{aligned} \quad (52)$$

201 The only difference from the problem (27) is that the test function  $w_h$  belongs to  $V_h^t$  instead of its subspace  $V_{h,0}^t$ . By  
 202 similar derivations in the previous section, we can derive the following Euler-Lagrange equation

$$\begin{cases} \frac{\partial \mathcal{E}_h}{\partial \rho_i} - \int_I \phi_i \lambda_h dx = 0, & i = 1, \dots, N-1; \\ \int_I \rho_h v_h \phi_i dx + \frac{\partial \mathcal{E}_h}{\partial x_i} - \int_I \psi_i \lambda_h dx + \int_I \rho_h \partial_x \lambda_h \phi_i dx = 0, & i = 0, \dots, N; \\ \int_I \partial_t \rho_h \phi_i dx - \int_I \rho_h v_h \partial_x \phi_i dx = 0, & i = 0, \dots, N. \end{cases} \quad (53)$$

203 In an algebraic form, the equation is rewritten as

$$\begin{cases} \widehat{\mathbf{M}}(\mathbf{x}(t)) \widehat{\lambda}(t) = \frac{\partial \mathcal{E}_h}{\partial \rho}(\mathbf{x}(t), \rho(t)), \\ \mathbf{D}(\mathbf{x}(t), \rho(t)) \dot{\mathbf{x}}(t) = -\frac{\partial \mathcal{E}_h}{\partial \mathbf{x}}(\mathbf{x}(t), \rho(t)) + (\widehat{\mathbf{B}}(\mathbf{x}(t)) - \widehat{\mathbf{E}}(\mathbf{x}(t), \rho(t)))^T \widehat{\lambda}(t), \\ \widehat{\mathbf{M}}^T(\mathbf{x}(t)) \dot{\rho}(t) + (\widehat{\mathbf{B}}(\mathbf{x}(t)) - \widehat{\mathbf{E}}(\mathbf{x}(t), \rho(t))) \dot{\mathbf{x}}(t) = 0, \end{cases} \quad (54)$$

where  $\mathbf{D}$  is the same as in (30),  $\widehat{\mathbf{M}} \in \mathbb{R}^{N-1, N+1}$ ,  $\widehat{\mathbf{B}} \in \mathbb{R}^{N+1, N+1}$ ,  $\widehat{\mathbf{E}} \in \mathbb{R}^{N+1, N+1}$  such that

$$\begin{aligned}\widehat{\mathbf{M}}_{ij}(\mathbf{x}(t)) &= \int_{I(t)} \phi_i \phi_j dx; & \widehat{\mathbf{B}}_{ij}(\mathbf{x}(t)) &= \int_{I(t)} \phi_i \psi_j dx; \\ \widehat{\mathbf{E}}_{ij}(\mathbf{x}(t), \boldsymbol{\rho}(t)) &= \int_{I(t)} \rho_h \partial_x \phi_i \phi_j dx.\end{aligned}$$

204 For the semi-discrete problem (53), we have the following proposition,

205 **Proposition 3.** *Under the assumptions (A1) and (A2), let  $\boldsymbol{\rho}(t)$ ,  $\mathbf{x}(t)$  be the solution of the equations (25) and (53), then*  
206 *the total mass is conserved in the sense that,*

$$\frac{d}{dt} \int_{I(t)} \rho_h(x, t) dx = 0. \quad (55)$$

*Proof.* Similar to the analysis in the proof in Proposition 2, we have

$$\frac{d}{dt} \int_{I(t)} \rho_h(x, t) \phi_i(x, t) dx = 0, \quad i = 0, \dots, N.$$

207 Noticing that  $\sum_{i=0}^N \phi_i = 1$ , the equation (55) is obtained by adding all the above equations together.  $\square$

We can also develop an explicit linear scheme and an implicit nonlinear scheme by time discretization. However, the explicit scheme is not decoupled in this case. The two schemes in algebraic forms are respectively given by,

$$\widehat{\mathbf{M}}^n \widehat{\boldsymbol{\lambda}}^{n+1} = \frac{\partial \mathcal{E}_h^n}{\partial \boldsymbol{\rho}^n}, \quad (56)$$

$$\mathbf{D}^n \mathbf{v}^{n+1} - (\widehat{\mathbf{B}}^n - \widehat{\mathbf{E}}^n)^T \boldsymbol{\lambda}^{n+1} = -\frac{\partial \mathcal{E}_h^n}{\partial \mathbf{x}^n}, \quad (57)$$

$$(\widehat{\mathbf{M}}^n)^T \bar{\partial} \boldsymbol{\rho}^n + (\widehat{\mathbf{B}}^n - \widehat{\mathbf{E}}^n) \mathbf{v}^{n+1} = 0; \quad (58)$$

and

$$\widehat{\mathbf{M}}^n \widehat{\boldsymbol{\lambda}}^{n+1} - \frac{\partial \mathcal{E}_h^{n+1}}{\partial \boldsymbol{\rho}^{n+1}} = 0, \quad (59)$$

$$\mathbf{D}^n \mathbf{v}^{n+1} - (\widehat{\mathbf{B}}^n - \widehat{\mathbf{E}}^n)^T \widehat{\boldsymbol{\lambda}}^{n+1} = -\frac{\partial \mathcal{E}_h^n}{\partial \mathbf{x}^n}, \quad (60)$$

$$(\widehat{\mathbf{M}}^n)^T \bar{\partial} \boldsymbol{\rho}^n + (\widehat{\mathbf{B}}^n - \widehat{\mathbf{E}}^n) \mathbf{v}^{n+1} = 0. \quad (61)$$

208 Although the semi-discrete scheme (53) satisfies the mass conservation property, the fully discrete schemes do not  
209 satisfy the property since they are linearized schemes. Our numerical experiments show that the numerical scheme  
210 (56)-(58)(or (59)-(61)) gives almost the same results as those in the previous section. Therefore, we will use the  
211 simpler schemes (45)-(47) and (48)-(50) in the numerical examples next section.

## 212 5. Numerical examples

213 In this section we present some numerical results to show the effectivity of our numerical methods. We consider  
214 both one dimensional and two dimensional problems.

215 We choose the Barenblatt-Pattle solution [?] to test the accuracy of our method. The Barenblatt-Pattle solution  
216 is a special solution for the PME in  $\mathbb{R}^d$ . Let  $\mathbf{x}$  be the coordinate of a point in  $\mathbb{R}^d$ . This solution has an explicit form

$$B(\mathbf{x}, t) = t^{-\alpha} (C - k|\mathbf{x}|^2 t^{-2\beta})_+^{\frac{1}{m-1}}, \quad (62)$$

where  $(s)_+ = \max\{s, 0\}$ ,

$$\alpha = \frac{d}{d(m-1)+2}, \quad \beta = \frac{\alpha}{d}, \quad k = \frac{\alpha(m-1)}{2md},$$

and  $d$  is the number of dimension,  $C > 0$  is a constant determined by the total mass. This solution has a compact support in space for any fixed time  $t$ . The free boundary is the surface given by the equation

$$t = c|\mathbf{x}|^{d(m-1)+2}, \quad (63)$$

where  $c = \left(\frac{k}{C}\right)^{\frac{d(m-1)+2}{2}}$ . The boundary position changes when  $t$  increases.

The  $L^2$  error between the discrete solution  $\rho_h$  and the exact solution  $\rho$  at time  $T$  is computed by

$$err_{L^2} := \left( \int_{\Omega} (\rho(\mathbf{x}, T) - \rho_h(\mathbf{x}, T))^2 d\mathbf{x} \right)^{1/2}. \quad (64)$$

### 5.1. One-dimensional problems

Numerical experiments show that both the explicit and implicit schemes work well when the time step is small. In the one-dimensional case, absent further specification, we employ the implicit scheme (39)-(41) to solve the PME. We are mainly interested in the adaptive motion of the mesh and how it affects the numerical errors.

#### 5.1.1. Convergence tests

We first consider the Barenblatt-Pattle solution, with constants  $C = 1$  and  $d = 1$ . We take the Barenblatt-Pattle solution at  $t = 1$ , denoted as  $B(x, 1)$ , as the initial data. We compare the numerical solution with the exact solution  $B(x, T)$  at time  $T = 2$ , for both  $m = 2$  and  $m = 5$  cases. To investigate the accuracy of the method in the one-dimensional case, we use a uniform mesh and a least square best fit mesh [?] for the initial data, respectively. In both cases, the number of intervals in the mesh is increased by a factor of two, and the time step is reduced by a factor of four to test the convergence rate.

Figure 1 shows the convergence behavior of our method in various situations. We set the initial time step  $\tau = 0.01$ . In the numerical tests, the time step is relatively small. The reason is that our method leads to non-uniform meshes in general, which is very fine near the boundary and coarse in the central region. This increases the stiffness of the semi-discrete problem. From Figure 1(a), we observe that when  $m = 2$ , the second-order convergence rate can be obtained on a uniform initial mesh. However, when  $m = 5$ , the uniform initial mesh leads to a slower convergence rate. This is due to the fact that larger  $m$  corresponds to a more singular solution of the PME. To cure the discrepancy of the convergence rate, we can choose a better initial mesh by finding a best approximation to the initial function in a piecewisely linear finite element space with free knots. We do this by a least square method [?]. The numerical results for the non-uniform initial meshes are shown in Figure 1(b). We see that the optimal convergence rate is obtained for both  $m = 2$  and  $m = 5$  cases. In Figure 1, we also illustrate the numerical results by using the method with the lumped mass matrix  $\bar{M}$  as discussed in Remark 1. The lumped mass method exhibits similar convergence behavior to the original method (39)-(41).

Figure 2 exhibits the numerical and exact (Barenblatt-Pattle) solutions at  $T = 2$  for  $m = 5$  using different meshes. We see that the numerical solutions fit well with the exact solution even for a very coarse mesh. This implies that the boundary points moves correctly when time evolves.

As stated in Section 3, the numerical scheme (29) does not preserve the total mass exactly. Nevertheless, numerical experiments show that the errors for the mass are usually small. Some typical results are listed in Table 1. Here we set  $C = \frac{3^{1/3}}{4}$  for  $m = 2$ , and  $C = 0.07808$  for  $m = 5$  to ensure the total mass  $\int_I B(x, 1) dx = 1$ . we see that the errors for the total mass are very small and decay with an optimal convergence rate.

#### 5.1.2. Comparisons of different methods

Then we conduct numerical comparisons for different schemes including the Lagrangian method presented in [?]. Specifically, we compare the  $L^2$  errors, convergence rates, and computation times for the one-dimensional porous media equation at  $T = 2$  in the cases  $m = 2$  and  $m = 5$ , under both uniform and non-uniform initial mesh discretizations. In this numerical comparison, both the Lagrangian scheme in [?] and the scheme (39)-(41) are implicit schemes, for which we employ the Newton iteration method to obtain solutions. The stopping criterion for the



Figure 1: Convergence of the numerical solutions for the PME ( $m = 2, 5$ ) at  $T = 2$ .

$N$	$\tau$	Error for $m = 2$	Order	Error for $m = 5$	Order
12	1/100	$5.5471 \times 10^{-4}$		$1.0078 \times 10^{-4}$	
24	1/400	$1.3884 \times 10^{-4}$	1.9983	$2.6645 \times 10^{-5}$	1.9193
48	1/1600	$3.4719 \times 10^{-5}$	1.9996	$6.9277 \times 10^{-6}$	1.9434
96	1/6400	$8.6804 \times 10^{-6}$	1.9999	$1.7764 \times 10^{-6}$	1.9634

257 Newton iteration is set as the norm of gradient less than  $10^{-6}$ , with a maximum of 100 iterations allowed. The explicit  
 258 scheme (33)-(35) permits the decoupling of equations, enabling the sequential solution of several linear systems. The  
 259 numerical experiments were performed on a MacBook Pro with a 2 GHz quad-core Intel Core i5 processor.

260 As illustrated in Table 2, for the case  $m = 2$ , all three methods achieve a second-order convergence rate under  
 261 uniform initial grid discretizations. However, in terms of computational efficiency, the explicit method is fastest  
 262 among all the three schemes since there is no need to solve a nonlinear algebraic equation. Meanwhile, our implicit  
 263 method costs more computation time than that of the Lagrange scheme in [? ], since our method has more unknowns  
 264 and we need to solve a much larger system. Table 3 demonstrates that, for  $m = 5$ , none of the three numerical schemes  
 265 attain second-order convergence rate when the initial mesh is uniform. The computational costs of the three schemes  
 266 are similar to the case when  $m = 2$ .

267 Table 4 and Table 5 present numerical results for  $m = 5$  with optimal non-uniform initial mesh. In this case, the  
 268 mesh size near the boundary is very small, leading to the fact that the semi-discrete dynamic systems are very stiff.  
 269 Table 4 shows that the Lagrange method in [? ] does not converge even when the time step is ten times smaller  
 270 than that of the uniform mesh case, while our methods work and exhibit good convergence behavior under the same  
 271 conditions. Table 5 shows that the stabilized numerical scheme (36)-(38) and the implicit scheme (39)-(41) work  
 272 when the time step is chosen as the same as that of the uniform mesh case (ten times larger than that in Table 4). The  
 273 decoupled explicit scheme (33)-(35) fails only when the number of grid points reaches 96. These results indicate



Figure 2: The exact solutions (red solid line) and the numerical solutions (blue circles) of the PME( $m = 5$ ).

274 that introducing more variables in our methods is helpful to deal with more singular problems in comparison with the  
 275 method in [? ]. The stabilized explicit method (36)-(38) seems to be the best choice among all these methods when  
 276 the parameter  $m$  is large. It is more stable than the decoupled explicit scheme (33)-(35) and costs less time than the  
 277 implicit scheme (39)-(41).

Table 2: The comparison of methods for  $m = 2$  at  $T = 2$  under the uniform initial mesh

$N$	$\tau$	The Lagrange method in [? ]			Explicit scheme (33)-(35)			Implicit scheme (39)-(41)		
		$L^2$ error	Order	Time (s)	$L^2$ error	Order	Time (s)	$L^2$ error	Order	Time (s)
12	1/100	0.0119		0.020204	0.0127		0.013264	0.0127		0.029935
24	1/400	0.0030	1.9879	0.043949	0.0032	1.9887	0.041757	0.0032	1.9887	0.187873
48	1/1600	7.4432e-4	2.0110	0.182364	7.9599e-4	2.0072	0.095804	7.9460e-4	2.0098	1.606934
96	1/6400	1.8595e-4	2.0010	1.450588	1.9900e-4	2.0000	0.602054	1.9828e-4	2.0027	13.055278



Table 3: The comparison of methods for  $m = 5$  at  $T = 2$  under the uniform initial mesh

$N$	$\tau$	The Lagrange method in [?] ]			Explicit scheme (33)-(35)			Implicit scheme (39)-(41)		
		$L^2$ error	Order	Time (s)	$L^2$ error	Order	Time (s)	$L^2$ error	Order	Time (s)
12	1/100	0.2721		0.025934	0.2356		0.019109	0.2269		0.074134
24	1/400	0.1616	0.7517	0.061532	0.1288	0.8712	0.063488	0.1238	0.8740	0.348429
48	1/1600	0.0960	0.7513	0.291109	0.0701	0.8776	0.231545	0.0677	0.8708	2.420672
96	1/6400	0.0571	0.7495	2.106921	0.0381	0.8796	1.709349	0.0372	0.8639	24.551611

Table 4: The comparison of methods for  $m = 5$  at  $T = 2$  under the non-uniform initial mesh

$N$	$\tau$	The Lagrange method in [?] ]			Explicit scheme (33)-(35)			Implicit scheme (39)-(41)		
		$L^2$ error	Order	Time (s)	$L^2$ error	Order	Time (s)	$L^2$ error	Order	Time (s)
12	1/1000	–	–	–	0.0500		0.089584	0.0513		0.339997
24	1/4000	–	–	–	0.0144	1.7959	0.333953	0.0151	1.7644	2.093960
48	1/16000	–	–	–	0.0044	1.7105	1.830398	0.0046	1.7148	21.903188
96	1/64000	–	–	–	0.0014	1.6521	13.466308	0.0015	1.6167	150.726021

Table 5: The comparison of methods for  $m = 5$  at  $T = 2$  under the non-uniform initial mesh

$N$	$\tau$	Explicit scheme (33)-(35)			Stablized explicit scheme (36)-(38)			Implicit scheme (39)-(41)		
		$L^2$ error	Order	Time (s)	$L^2$ error	Order	Time (s)	$L^2$ error	Order	Time (s)
12	1/100	0.0495		0.050430	0.0514		0.031399	0.0518		0.079790
24	1/400	0.0143	1.7914	0.055470	0.0152	1.7577	0.155128	0.0153	1.7577	0.229261
48	1/1600	0.0058	1.3019	0.239831	0.0046	1.7244	1.181074	0.0046	1.7244	2.767125
96	1/6400	–	–	–	0.0015	1.6167	10.685654	0.0015	1.6167	34.953982

### 5.1.3. Waiting time phenomenon

It is known that the solution of the PME may exhibit a waiting time phenomenon. Namely the support of the solution may not change until the time  $t$  is larger than some critical value  $t^*$ . To test if our method can capture this phenomenon, we consider an initial value as in [? ],

$$\rho_0(x) = \begin{cases} \left( \frac{m-1}{m} ((1-\theta) \sin^2(x) + \theta \sin^4(x)) \right)^{\frac{1}{m-1}}, & x \in [-\pi, 0], \\ 0, & \text{otherwise,} \end{cases} \quad (65)$$

with  $\theta \in [0, 1]$ . For such an initial value, the critical waiting time is given by an explicit formula  $t^* = \frac{1}{2(m+1)(1-\theta)}$  when  $\theta \in [0, \frac{1}{4}]$ .

In our tests, we set  $\theta = 0$  and  $m = 4$ . This gives a waiting time  $t^* = 0.1$ . Here we set  $N = 48$  and  $\tau = 2.5 \times 10^{-3}$ . The numerical solutions at various time are shown in Figure 3. We see that the shape of the solution changes while the support of the solution does not change until  $t \geq 0.1$ . To show the motion of the boundary points more clearly, we plot the coordinates of the left and right boundaries with respect to time in Figure 4. Here we choose various values for the parameters  $\theta$  and  $m$ . For  $m = 4$ , we set  $\theta = 0$  and  $1/5$ . The waiting time is 0.1 and 0.125, respectively. For  $m = 5$ , we set  $\theta = 1/6$  and the according waiting time is 0.1. From Figure 4, we can observe that our numerical method can automatically capture the waiting time phenomenon for all these cases.

### 5.2. Two-dimensional problems

We apply our numerical method to the PME in two dimensions. The explicit formulae of the numerical schemes are given in the appendix. In the numerical tests, we use the explicit numerical scheme for simplicity. In 2D, the convergence rate  $p$  is calculated by

$$p = \frac{\log(err_1/err_2)}{\log(\sqrt{N_2}/N_1)}, \quad (66)$$

where  $err_1$  and  $err_2$  are the  $L^2$  errors for the numerical solutions calculated on meshes with  $N_1$  and  $N_2$  vertexes, respectively.



Figure 3: Numerical solutions of the PME ( $m = 4$ ) with the initial value (65) with  $\theta = 0$ . Here  $N = 48$ ,  $\tau = 2.5 \times 10^{-3}$ .

297 *5.2.1. Convergence test*

298 We consider the two dimensional Barenblatt-Pattle solution  $B(x, y, t)$  with  $C = 0.1$  and  $d = 2$ , where  $(x, y)$  is the  
 299 coordinate of a point in  $\mathbb{R}^2$ . We set  $B(x, y, 1)$  as the initial data and test the convergence rate at  $T = 2$ . The numerical  
 300 results are shown in Figure 5. The numerical results are similar to that in one dimensional case. We see that the  
 301 optimal convergence rate is obtained when  $m = 2$  with a quasi-uniform initial mesh. For larger  $m$ , the uniform initial  
 302 mesh will lead to a sub-optimal convergence rate. This is shown in Figure 5 for the  $m = 5$  case. We also see that that  
 303 the convergence rate is better on a non-uniform initial mesh than that on a uniform one. We remark that it is not an  
 304 easy task to find an optimal initial mesh in 2D as discussed in [? ].

305 We can also compute the waiting time phenomenon in the two dimensional case. For that purpose, we choose

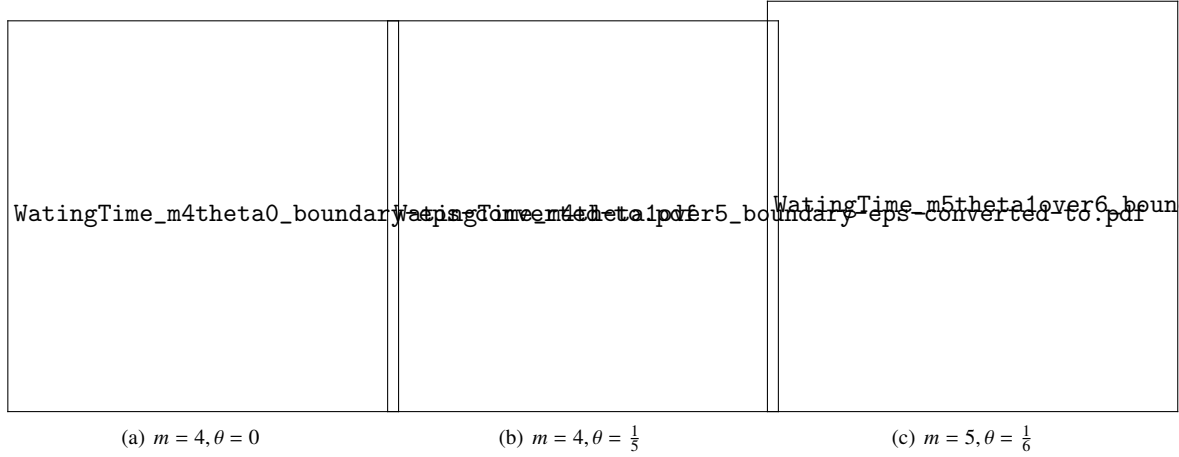


Figure 4: Boundaries motion of the PME for different  $m$  and  $\theta$ .

306  $m = 2$  and the following initial function,

$$\rho_0(x, y) = \begin{cases} \frac{1}{2} \sin^2(\sqrt{x^2 + y^2} - \pi), & \text{if } \sqrt{x^2 + y^2} \leq \pi, \\ 0, & \text{otherwise.} \end{cases} \quad (67)$$

307 According to the previous theoretical results [? ], there exists a positive waiting time for such an initial value. In  
 308 the numerical test, the initial triangulation for  $\Omega := \{(x, y) : \sqrt{x^2 + y^2} < \pi\}$  is quasi-uniform with 1983 cells. We set  
 309  $\tau = 10^{-3}$ .

310 Figure 6 shows the numerical solutions of the PME for the initial data (67) at various time. We see that the  
 311 numerical method can also capture the waiting time phenomenon very well in the two dimensional case and the  
 312 waiting time is about 0.125.

### 313 5.2.2. General examples

314 Finally, we show some examples with more general initial values. We first consider an initial value with a  
 315 compact support of ‘‘horseshoe’’ shape, as in [? ? ?]. In the test, we set  $m = 2$  and the initial function is given by

$$\rho_0(x, y) = \begin{cases} 50(0.25^2 - (\sqrt{x^2 + y^2} - 0.75)^2)^2, & \text{if } \sqrt{x^2 + y^2} \in (0.5, 1) \text{ and } (x < 0 \text{ or } y < 0); \\ 50(0.25^2 - x^2 - (y - 0.75)^2)^2, & \text{if } x^2 + (y - 0.75)^2 \leq 0.25^2 \text{ and } x \geq 0; \\ 50(0.25^2 - (x - 0.75)^2 - y^2)^2, & \text{if } (x - 0.75)^2 + y^2 \leq 0.25^2 \text{ and } y \leq 0; \\ 0, & \text{otherwise.} \end{cases} \quad (68)$$

316 Figure 7 illustrates how the solution evolves with time. We see our method can solve the problem very well until the  
 317 boundary of the support intersecting each other. However, the present numerical method cannot directly deal with the  
 318 topology change.

319 To deal with the topology change, a possible way is to consider a regularized problem where the PME is extended  
 320 to a larger region and the initial value is set to be a small positive constant in the outer region. In the following, we  
 321 show such an example with a solution with two peaks merging into one for the PME with  $m = 3$ , motivated by the  
 322 work in [? ?]. Let  $\Omega = [-1.5, 1.5]^2$  and the initial data is given by

$$\rho_0(x, y) = e^{-20*((x-0.3)^2+(y-0.3)^2)} + e^{-20*((x+0.3)^2+(y+0.3)^2)} + 0.001, \quad (69)$$



Figure 5: Convergence of the numerical solutions of the PME ( $m = 2, 5$ ) at  $T = 2$ .



Figure 6: Numerical solutions of the PME( $m = 2$ ) with the initial value (67).

323 which has two peak regions connected by a very thin layer with thickness 0.001. The numerical results are shown in  
 324 Figure 8. It is clearly seen that the two separate peaks merges together gradually.

## 325 6. Conclusion

326 In this paper, we utilize the Onsager principle to develop a new moving mesh method for the porous medium equa-  
 327 tion. We demonstrate that both the continuous PME and a semi-discrete scheme can be derived using this principle,  
 328 ensuring that the scheme maintains the same energy dissipation structure as the continuous problem. Additionally,  
 329 we introduce a fully discrete explicit decoupled scheme and an implicit scheme. Numerical examples illustrate the  
 330 effectiveness of both schemes, showing that optimal convergence rates for the  $L^2$  error can be achieved when the initial

331 meshes are appropriately selected. The method naturally captures the waiting time phenomena and can be extended to  
 332 higher-dimensional problems and higher-order approximations. It is important to note that while the derivation of the  
 333 method is intuitive, the error estimate for the moving mesh method remains an open question. Optimal convergence  
 334 estimates will require suitable assumptions regarding the initial meshes and the regularity properties of the system.

### 335 Acknowledgment

336 The authors thank the anonymous referees for valuable comments which help us to improve the manuscript.

### 337 Declaration of generative AI and AI-assisted technologies in the writing process

338 During the preparation of this work the authors used DeepSeek and ChatGPT 3.5 in order to improve the English  
 339 writing and readability of some part of the paper. After using this tool/service, the authors reviewed and edited the  
 340 content as needed and take full responsibility for the content of the published article.

### 341 Appendix A. Numerical scheme in two dimensions

342 In this appendix, we will give the discrete numerical scheme in the two dimensional case. Let  $\Omega(t) \subset \mathbb{R}^2$  be the  
 343 domain where the PME is defined. Denote by  $\mathcal{T}_h$  a partition of  $\Omega$  with  $N_K$  disjoint triangles  $K$  such that the union of  
 344 the triangles compose a polygonal domain  $\Omega_h$ . We suppose that the boundary vertices of  $\Omega_h$  locate on  $\partial\Omega$  initially.  
 345 Let  $V_h^t$  be the finite element space with respect to the mesh  $\mathcal{T}_h$ ,

$$V_h^t := \{u_h \in C(\bar{\Omega}_h) | u_h \text{ is linear in } K_i, i = 1, \dots, N_K\}. \quad (\text{A.1})$$

Let  $N_{in}$  be the number of vertices inside  $\Omega_h$ , and let  $N$  be the total number of the vertexes in  $\bar{\Omega}_h$ . Denote by  $P_j = (x_j, y_j)$ ,  
 $j = 1, \dots, N$ , a vertex of  $\mathcal{T}_h$  which may change position with time  $t$ . Denote by

$$V_{h,0}^t = \{u_h \in V_h^t : u_h(P_j) = 0, \forall P_j \text{ on } \partial\Omega_h\}.$$

Then the approximation  $\rho_h(x, y, t) = \sum_{i=1}^{N_{in}} \rho_k(t) \phi_i(x, y, t)$ , where  $\phi_k(x, y, t), i = 1, \dots, N_{in}$  are the global piecewisely  
 linear finite element basis functions. Similar to the one-dimensional case, the time derivative and space derivative of  
 $\rho_h(x, y, t)$  are given by

$$\begin{aligned} \partial_t \rho_h &= \sum_{i=1}^{N_{in}} \dot{\rho}_i(t) \phi_i(x, y, t) + \sum_{i=1}^N (\dot{x}_i(t) \psi_{x,i}(x, y, t) + \dot{y}_i(t) \psi_{y,i}(x, y, t)), \\ \partial_x \rho_h &= \sum_{i=1}^{N_{in}} \rho_i(t) \partial_x \phi_i(x, y, t), \\ \partial_y \rho_h &= \sum_{i=1}^{N_{in}} \rho_i(t) \partial_y \phi_i(x, y, t), \end{aligned}$$

where

$$\psi_{x,i} = \frac{\partial \rho_h}{\partial x_i}, \quad \psi_{y,i} = \frac{\partial \rho_h}{\partial y_i}.$$

346 Denote by  $\boldsymbol{\rho} = (\rho_1(t), \dots, \rho_{N_{in}}(t))^T$ ,  $\mathbf{x} = (x_1(t), \dots, x_N(t))^T$  and  $\mathbf{y} = (y_1(t), \dots, y_N(t))^T$ , then the discrete energy functional  
 347  $\mathcal{E}$  and its time derivative are respectively given by

$$\mathcal{E}_h(\boldsymbol{\rho}, \mathbf{x}, \mathbf{y}) = \int_{\Omega_h} f(\rho_h) dx dy \quad (\text{A.2})$$

348 and

$$\dot{\mathcal{E}}_h(\boldsymbol{\rho}, \mathbf{x}, \mathbf{y}; \dot{\boldsymbol{\rho}}, \dot{\mathbf{x}}, \dot{\mathbf{y}}) = \sum_{i=1}^{N_m} \frac{\partial \mathcal{E}_h}{\partial \rho_i} \dot{\rho}_i + \sum_{i=1}^N \left( \frac{\partial \mathcal{E}_h}{\partial x_i} \dot{x}_i + \frac{\partial \mathcal{E}_h}{\partial y_i} \dot{y}_i \right), \quad (\text{A.3})$$

where

$$\begin{aligned} \frac{\partial \mathcal{E}_h}{\partial \rho_i} &= \int_{\Omega_h} f'(\rho_h) \phi_i dx dy, \quad i = 1, \dots, N_m; \\ \frac{\partial \mathcal{E}_h}{\partial x_i} &= \int_{\Omega_h} f'(\rho_h) \psi_{x,i} dx dy, \quad i = 1, \dots, N; \\ \frac{\partial \mathcal{E}_h}{\partial y_i} &= \int_{\Omega_h} f'(\rho_h) \psi_{y,i} dx dy, \quad i = 1, \dots, N. \end{aligned}$$

Let  $\mathbf{v}_h(x, y, t) = (v_x^h(x, y, t), v_y^h(x, y, t))$  be an approximation of velocity  $\mathbf{v}$ , s.t.  $v_x^h(x, y, t) = \sum_{i=1}^N v_{x,i}(t) \phi_i(x, y, t)$  and  $v_y^h(x, y, t) = \sum_{i=1}^N v_{y,i}(t) \phi_i(x, y, t)$ . Let  $\lambda_h(x, y, t) = \sum_{i=1}^{N_m} \lambda_i(t) \phi_i(x, y, t)$  be an approximation of  $\lambda(x, y, t)$ . Then we can obtain a discrete version of the dissipation function,

$$\Phi_h = \frac{1}{2} \int_{\Omega_h} \rho_h |\mathbf{v}_h|^2 dx dy = \frac{1}{2} \int_{\Omega_h} \rho_h (v_{x,h}^2 + v_{y,h}^2) dx dy.$$

For the continuum equation, we have

$$\begin{aligned} \sum_{K \in \mathcal{T}_h} \int_K [\partial_t \rho_h + \nabla \cdot (\rho_h \mathbf{v}_h)] w_h dx dy &= \sum_{K \in \mathcal{T}_h} \int_K (\partial_t \rho_h w_h - \rho_h \mathbf{v}_h \cdot \nabla w_h) dx dy \\ &= \int_{\Omega_h} (\partial_t \rho_h w_h - \rho_h (v_{x,h} \partial_x w_h + v_{y,h} \partial_y w_h)) dx dy = 0, \quad \forall w_h \in V_{h,0}^t. \end{aligned}$$

349

Then we have the discrete Rayleighian functional with a Lagrange multiplier  $\lambda_h$ ,

$$\tilde{\mathcal{R}}_h = \Phi_h + \dot{\mathcal{E}}_h - \int_{\Omega_h} \partial_t \rho_h \lambda_h - \rho_h (v_{x,h} \partial_x \lambda_h + v_{y,h} \partial_y \lambda_h) dx dy. \quad (\text{A.4})$$

We directly compute the corresponding Euler-Lagrange equations,

$$\frac{\partial \tilde{\mathcal{R}}_h}{\partial \dot{\rho}_i} = \frac{\partial \mathcal{E}_h}{\partial \rho_i} - \int_{\Omega_h} \phi_i \lambda_h dx dy = 0, \quad i = 1, \dots, N_m; \quad (\text{A.5})$$

$$\frac{\partial \tilde{\mathcal{R}}_h}{\partial v_{x,i}} = \int_{\Omega_h} \rho_h v_{x,h} \phi_i dx dy + \frac{\partial \mathcal{E}_h}{\partial x_i} - \int_{\Omega_h} \psi_{x,i} \lambda_h dx dy + \int_{\Omega_h} \rho_h \phi_i \partial_x \lambda_h dx dy = 0, \quad i = 1, \dots, N; \quad (\text{A.6})$$

$$\frac{\partial \tilde{\mathcal{R}}_h}{\partial v_{y,i}} = \int_{\Omega_h} \rho_h v_{y,h} \phi_i dx dy + \frac{\partial \mathcal{E}_h}{\partial y_i} - \int_{\Omega_h} \psi_{y,i} \lambda_h dx dy + \int_{\Omega_h} \rho_h \phi_i \partial_y \lambda_h dx dy = 0, \quad i = 1, \dots, N; \quad (\text{A.7})$$

$$\frac{\partial \tilde{\mathcal{R}}_h}{\partial \lambda_i} = \int_{\Omega_h} \partial_t \rho_h \phi_i + \rho_h (v_{x,h} \partial_x \phi_i + v_{y,h} \partial_y \phi_i) dx dy = 0, \quad i = 1, \dots, N_m. \quad (\text{A.8})$$

The equation can be written in an algebraic form as

$$\begin{aligned}
M\lambda &= \frac{\partial \mathcal{E}_h}{\partial \rho}, \\
D\mathbf{v}_x &= -\frac{\partial \mathcal{E}_h}{\partial \mathbf{x}} + (\mathbf{B}_x - \mathbf{E}_x)^T \lambda, \\
D\mathbf{v}_y &= -\frac{\partial \mathcal{E}_h}{\partial \mathbf{y}} + (\mathbf{B}_y - \mathbf{E}_y)^T \lambda, \\
M\dot{\rho} &= -(\mathbf{B}_x - \mathbf{E}_x)\mathbf{v}_x - (\mathbf{B}_y - \mathbf{E}_y)\mathbf{v}_y,
\end{aligned}$$

where

$$\begin{aligned}
M_{ij} &= \int_{\Omega_h} \phi_i \phi_j dx dy; & D_{ij} &= \int_{\Omega_h} \rho_h \phi_i \phi_j dx dy; \\
B_{x,ij} &= \int_{\Omega_h} \phi_i \psi_{x,j} dx dy; & B_{y,ij} &= \int_{\Omega_h} \phi_i \psi_{y,j} dx dy; \\
E_{x,ij} &= \int_{\Omega_h} \rho_h \partial_x \phi_i \phi_j^n dx dy; & E_{y,ij} &= \int_{\Omega_h} \rho_h \partial_y \phi_i \phi_j^n dx dy.
\end{aligned}$$

350 Similarly to the one dimensional case, we can further discretize the time derivative in the above system by an explicit  
351 Euler scheme or an implicit linearized scheme. We neglect the details for simplicity in presentation.

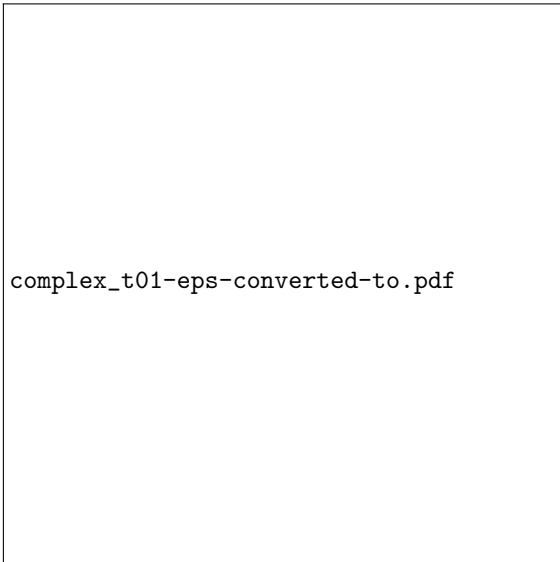




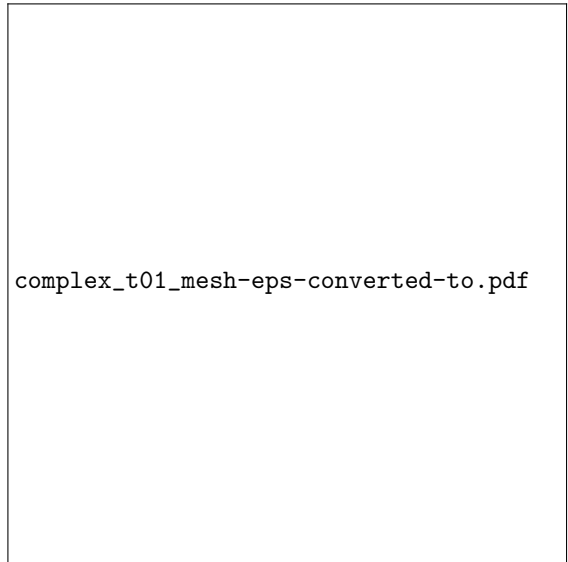
(a)  $t=0$



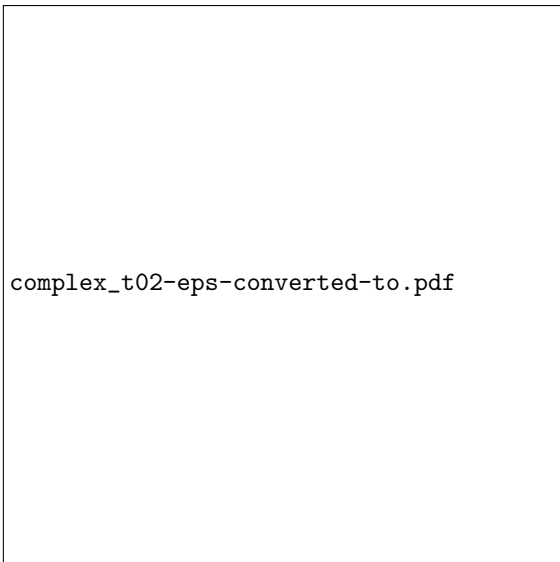
(b)  $t=0$



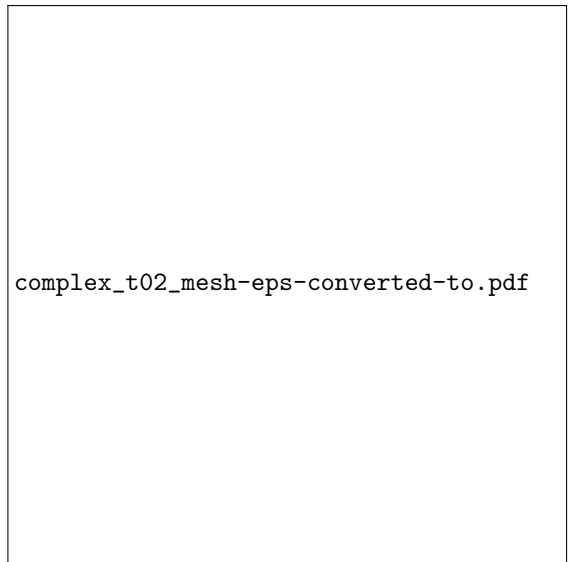
(c)  $t=0.1$



(d)  $t=0.1$

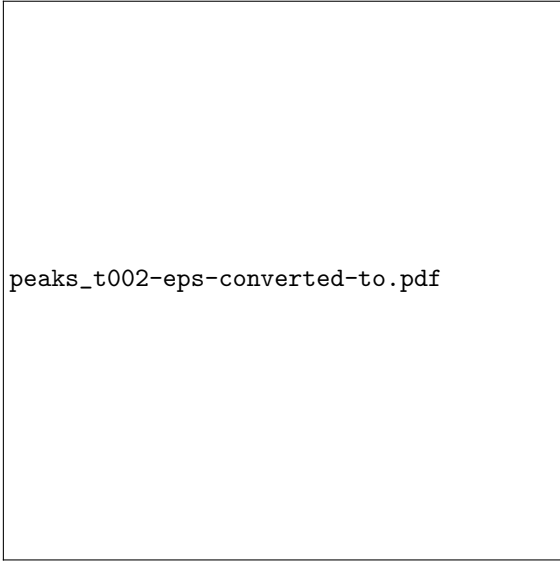


(e)  $t=0.2$

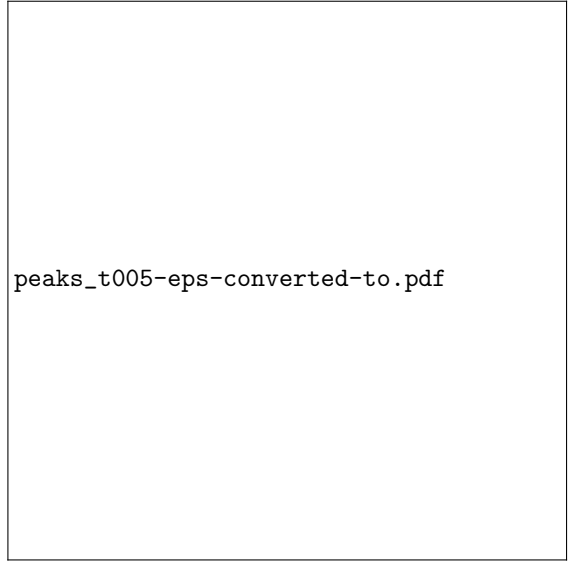


(f)  $t=0.2$

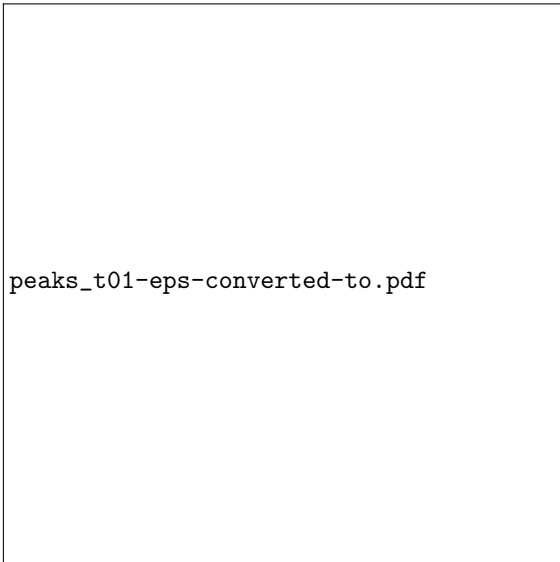
Figure 7: Numerical solutions of the PME( $m = 2$ ) with initial value (68). The initial mesh is quasi-uniform and has 910 nodes, 1684 cells. The time step is  $\tau = 10^{-3}$ .



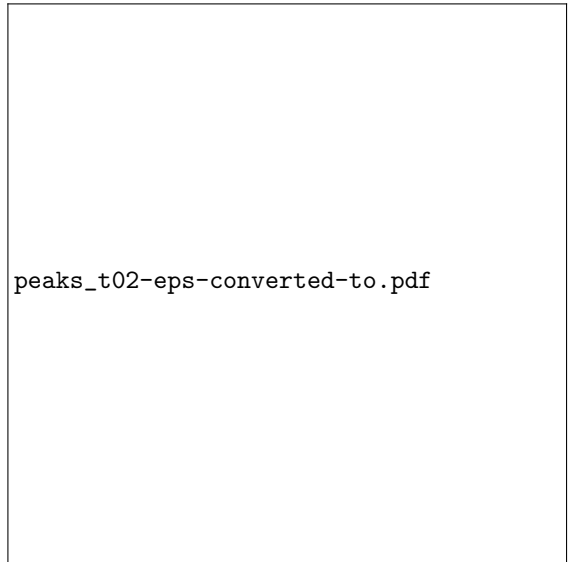
(a)  $t=0.02$



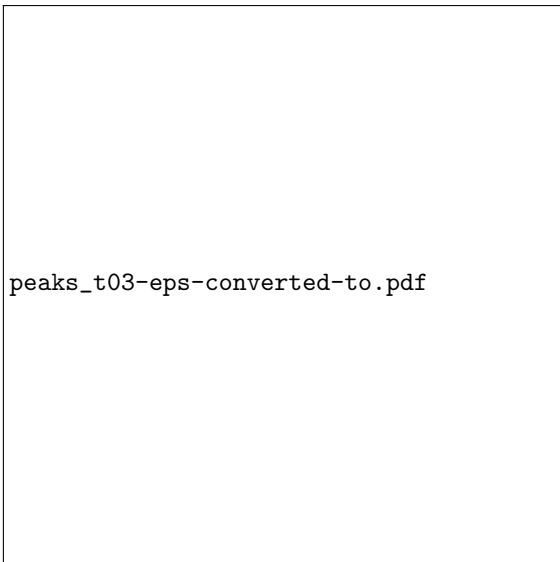
(b)  $t=0.05$



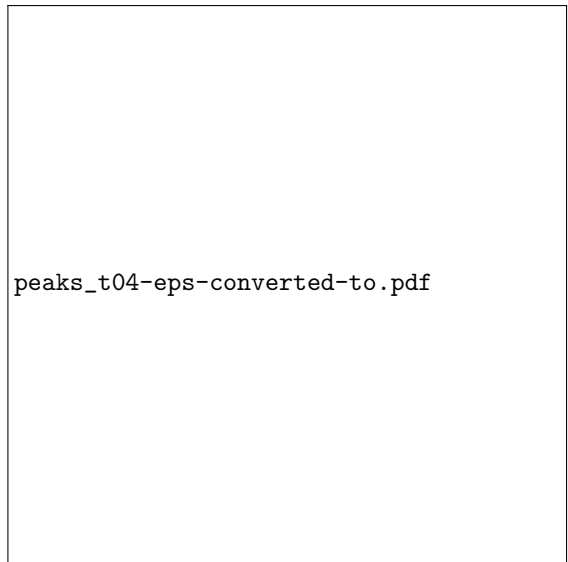
(c)  $t=0.1$



(d)  $t=0.2$



(e)  $t=0.3$



(f)  $t=0.4$

Figure 8: The numerical solutions for the PME ( $m = 3$ ) with initial value (69). The initial mesh is uniform with 961 nodes, 1800 cells. The time step is  $\tau = 10^{-3}$ .